In Silico Experiments to Explore the Heating Efficiency of Magnetic Nanoparticles in Hyperthermia Preclinical Tests

ADVANCED THEORY AND SIMULATIONS
www.advtheorysimul.com

In Silico Experiments to Explore the Heating Efficiency of Magnetic Nanoparticles in Hyperthermia Preclinical Tests

Marta Vicentini, Riccardo Ferrero, and Alessandra Manzin*

Preclinical tests on murine models are typically performed to evaluate the therapeutic efficacy of novel magnetic nanoparticles (MNPs) in cancer treatment with magnetic hyperthermia. Here, through in silico experiments, in vivo tests are mimicked on a 30 g mouse and a 500 g rat, with the aim of determining the optimal treatment conditions allowing to reach the therapeutic temperature range (40–45 °C) within tumor regions. Various types of MNPs are considered with very different heating properties in terms of specific loss power, varying their administered dose, as well as the frequency and peak amplitude of the magnetic field. The analysis is performed by means of finite element models that solve the low-frequency electromagnetic (EM) field problem and the Pennes' bioheat transfer equation, to calculate the temperature increase in biological tissues due to the combined effects of EM field exposure and MNP activation. The methodology, which can be generalized to any type of MNPs, has permitted to identify the proper doses of MNPs to be administered to the tumor region, as a function of their heating properties and magnetic field parameters, highlighting the conditions that can lead to possible overheating, generation of hot spots or magnetic hyperthermia inefficacy.

1. Introduction

In oncology, hyperthermia has been investigated as an adjuvant to radiotherapy or chemotherapy for the treatment of several cancer types, including brain, breast, liver, prostate, and lung. The reaching of a target temperature in the tumor mass, within the range of 40–45 °C, contributes to tumor cell damage and enhances cell sensitivity to standard therapies; moreover, adverse effects on healthy cells are reduced due to their lower susceptibility to temperature increase.[1–4]

Thanks to the latest advances in nanotechnology, magnetic hyperthermia has become a promising candidate for hyperthermia, due to the possibility of achieving highly selective heating. With this technique, magnetic nanoparticles (MNPs) excited by an alternating current (AC) magnetic field can lead to a localized release of heat in the tumor-affected region with limited side effects in the surrounding healthy tissues.[5–8] The MNP heating efficiency is generally measured by means of the specific loss power (SLP), which is defined as the power dissipated per unit mass of magnetic material, and can be estimated via thermometric or calorimetric measurements;[9,10] the SLP depends on the physicochemical, structural, and dimensional properties of MNPs (material composition, size, shape, and surface coating),[11–14] as well as on the AC magnetic field parameters (peak amplitude $\hat{H}_a$ and frequency f).[15,16] For a specific sample of MNPs, larger SLP values can be obtained by increasing $\hat{H}_a$ and/or f. However, the magnetic field parameters have to be selected within a range that satisfies biophysical constraints, to avoid undesired eddy current heating. A first indication, known as the Atkinson-Brezovich limit, was provided in 1984, that is $\hat{H}_a \times f \leq 4.85 \times 10^8$ A m^{-1} s^{-1};[17] a less rigid limit was introduced by Hergt and Dutz in 2007, that is $\hat{H}_a \times f \leq 5 \times 10^9$ A m^{-1} s^{-1}.[18]

A crucial aspect when planning magnetic hyperthermia treatments is the monitoring of the temperature increase, considering that the target temperature range should be ideally reached in the entire tumor region and maintained for a sufficiently long time (from 20–30 min up to 1 h). However, a complete knowledge of the temperature distribution within the region of interest is impossible during hyperthermia sessions. Typically, infrared thermal cameras are employed for the real-time monitoring of superficial temperature, whereas fiber-optic thermometers are used for the measurement of temperature in the target region, but this procedure can provide temperature values at discrete points only and can be rather invasive.[19–21]

Temperature measurements can be complemented by in silico modeling,[22] which can be used to evaluate the spatial-temporal distribution of the temperature in the target region, versus the MNP heating properties (SLP), the AC magnetic field parameters, the duty cycle, the MNP local concentration, as well as the position of the tumor within the body and its thermal properties. In silico replication of in vivo tests mainly focuses on the role of the MNP concentration and deposition pattern, and of the tumor size, shape, position, and thermal properties, giving

M. Vicentini, R. Ferrero, A. Manzin
Istituto Nazionale di Ricerca Metrologica (INRIM)
Strada delle Cacce 91, Torino 10135, Italy
E-mail: m.vicentini@inrim.it

The ORCID identification number(s) for the author(s) of this article can be found under https://doi.org/10.1002/adts.202300234

DOI: 10.1002/adts.202300234

less attention to the role of the type of employed MNPs and their ability to release heat as a function of magnetic field peak amplitude and frequency.[23–34] Moreover, to reduce computational complexity, most numerical models introduce simplifications on the body anatomy, which is often approximated as a domain composed of elementary regions, typically spherical, ellipsoidal, or cubic, where the inner one represents the tumor.[24–29] Further complexity is added, by considering a more realistic shape of the diseased organ, but describing the tumor as an internal sphere and avoiding the presence of surrounding healthy organs and tissues.[30] To better mimic in vivo tests and include the effects of thermal diffusion and heat exchange with the external environment, computational phantoms with realistic anatomical details are also employed, extending their volume to the tissues surrounding the diseased organ or to the entire body.[31–33] In some studies, the irregularities in the tumor shape are also included in the voxel discretization, via 3D reconstruction from in vivo measurements.[22,34]

In this framework, we present a physics-based modeling approach to evaluate the spatial distribution of the temperature increase induced by magnetic hyperthermia in tumor regions located in the body of two murine models (i.e., a 30 g mouse and a 500 g rat). Among the key factors that influence magnetic hyperthermia efficacy, we investigate the role of MNP heating properties (SLP) as a function of magnetic field parameters, in order to determine the optimal therapeutic conditions. In particular, we simulate hyperthermia treatments with four types of MNPs, varying the magnetic field peak amplitude $\hat{H}_a$ and frequency f, and the concentration of MNPs in the target region, where they are assumed to be uniformly distributed.

The spatial distribution of the temperature in the whole animal body is calculated by means of an in-house finite element method (FEM) code, developed to solve the Pennes' bioheat equation.[32,35] The numerical model takes into account the heating power due to MNP excitation as well as to AC magnetic field exposure. The latter term is calculated with an in-house FEM code that solves the low-frequency electromagnetic (EM) field problem, developed to assess possible eddy current effects.[35] To extend the parametric analysis, the results from thermal simulations are integrated with the outputs of regression models.

2. Results and Discussion

The modeling approach described in Section 4 is employed to simulate in vivo tests of magnetic hyperthermia, calculating the spatial distribution of temperature consequent to MNP excitation within voxel-based murine models. Specifically, we use the computational anatomical model of the Sprague Dawley rat available on the IT'IS Foundation database;[36] this model corresponds to a female rat with a weight of 503 g and a body length of 22.5 cm (excluding tail). Among the three tumors present in the animal, we assume that the MNPs are administered in the largest one (target region Σ), which has a size of $2.4 \times 3.7 \times 3.8$ cm^3 (corresponding to 3.1% of the body), and is located on the right flank (see schematic in **Figure 1**a). To also simulate the thermal response in a mouse-size model with a weight of about 30 g, we resize the rat model by a factor of 2.6. The tissue properties (electrical conductivity σ, density ρ, heat capacity C_p, thermal conductivity k, perfusion rate W, and metabolic heat Q_m) are extracted from the IT'IS Foundation database,[37] except for the tumor properties. Specifically, for the tumor regions σ is set at 0.8 S m^{-1},[38] ρ at 1045 kg m^{-3}, C_p at 3760 J K^{-1} kg^{-1}, k at 0.51 W K^{-1} m^{-1}, W at 9.97 kg s^{-1} m^{-3}, and Q_m at 31 872.5 W m^{-3}.[25] To simulate a condition where free convection is predominant, the heat transfer coefficient h is fixed to 3.5 W m^{-2} K^{-1}.[38] Being the animals generally anesthetized during magnetic hyperthermia tests, we assume that their thermoregulatory response is inactivated and thus we neglect the dependence of blood perfusion on temperature.[39]

We simulate different experimental conditions by considering four types of MNPs and by varying their dose within the treated tumor as well as the peak amplitude and frequency of the AC magnetic field. This is assumed to be uniformly distributed within the whole animal body, applied along its longitudinal axis, and with peak amplitude and frequency guaranteeing the fulfilment of the Hergt-Dutz limit.[18] The considered MNPs refer to samples available from the literature and previously characterized, via calorimetric heating measurements, in terms of SLP values versus $\hat{H}_a$ and f.[16] These comprise: 1) Johns Hopkins University (JHU) NPs from NanoMaterials Technology Pte Ltd (Singapore), composed of a multicrystallite dense iron oxide core stabilized with citrate;[16,40] 2) bionized nanoferrite (BNF) nanoparticles (NPs) from micromod Partikeltechnologie GmbH (Rostock, Germany), composed of a multicrystallite dense iron oxide core coated with a dextran shell;[16,41] 3) custom-made manganese ferrite NPs, composed of a multicrystallite dense iron-manganese oxide core stabilized with citrate;[16,42] and 4) Nanomag-D NPs from micromod Partikeltechnologie GmbH, composed of superparamagnetic iron oxide (SPIO) NPs dispersed in a dextran matrix.[16,41] According to the order above, we name the four types of MNPs as: 1) FeO@citrate NPs, 2) FeO@dextran NPs, 3) MnFeO@citrate NPs, and 4) SPIO@dextran NPs. We extrapolate the SLP values from the literature[16] for two frequencies, i.e., 150 and 300 kHz; Figure 1b–e shows the curves of the SLP versus the AC magnetic field peak amplitude $\hat{H}_a$ obtained via polynomial fitting.

2.1. Evaluation of Eddy Current Effects

Before the evaluation of the temperature increase caused by the MNP activation, we investigate heating phenomena due to the only EM field exposure. These can contribute to an additional temperature rise in the target region as well as to possible side effects in healthy tissues.[35] **Figure 2**a,b illustrates the effects of the AC magnetic field in the rat body as a function of the product $\hat{H}_a \times f$, reporting, respectively, the whole-body average specific absorption rate (SAR), and the average temperature T_{avg} and maximum temperature T_{max} in the body and in the target region Σ (the corresponding graphs for the mouse are reported in Figure S1, Supporting Information). The whole-body average SAR is calculated as

$$\mathrm{SAR} = \frac{1}{V_b} \int_{\Omega_b} \frac{\sigma |\mathbf{E}|^2}{2\rho} \mathrm{d}v \tag{1}$$

where V_b is the body volume and $\mathbf{E}$ is the electric field vector, which is estimated by means of the 3D FEM code used for

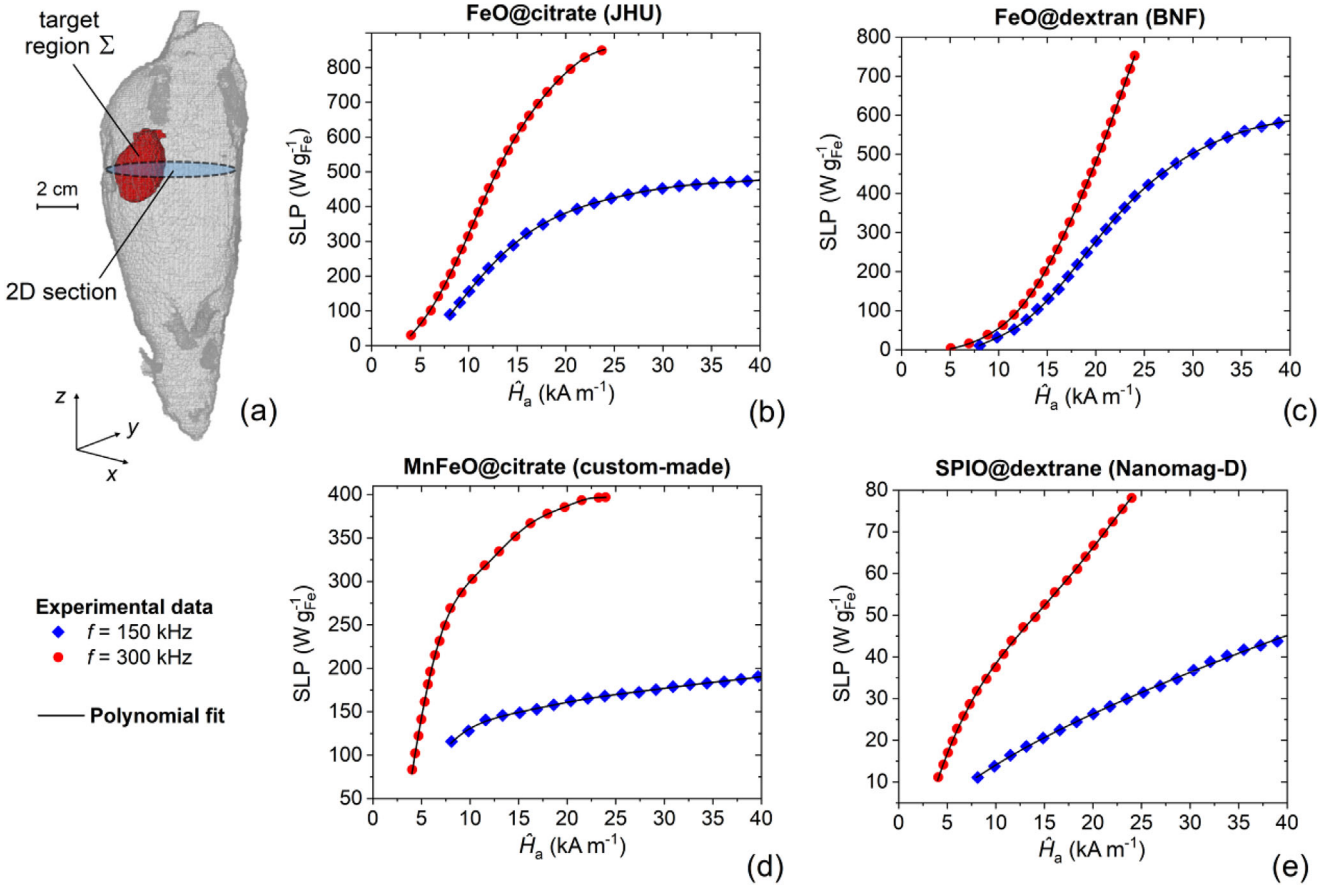

Figure 1. a) Schematic of the rat model with the target region Σ, where MNPs are administered, in red. Specific loss power (SLP) versus AC magnetic field peak amplitude for two frequencies (150 and 300 kHz), for b) FeO@citrate (JHU) NPs, c) FeO@dextran (BNF) NPs, d) custom-made MnFeO@citrate NPs, and e) SPIO@dextran (Nanomag-D) NPs. The blue and red markers correspond to the experimental data extrapolated from the literature,[16] whereas the black curves to their polynomial interpolation.

obtaining Q_{EM} in Equation (2).[35] The values of T_{avg} and T_{max} are determined at thermal equilibrium, reached in approximately 20 min. Nonappreciable increments of temperature are found in the mouse (Figure S1, Supporting Information), while non-negligible eddy current effects occur in the rat when the product $\hat{H}_a \times f$ exceeds the value of 3×10^9 A m^{-1} s^{-1}, i.e., for $\hat{H}_a$ = 20 kA m^{-1} when f = 150 kHz and $\hat{H}_a$ = 10 kA m^{-1} when f = 300 kHz. In these cases, average temperature increases larger than 0.9 and 0.3 °C are found in the body and in the target region, respectively, with a whole-body average SAR higher than 4 W kg^{-1}, value assumed as the threshold below which adverse effects due to EM field exposure would not be expected.[43]

When approaching the Hergt-Dutz limit, setting $\hat{H}_a \times f$ at 4.5×10^9 A m^{-1} s^{-1}, the temperature reaches a maximum of about 42 and 40 °C in the body and in the target region, respectively, corresponding to a whole-body average SAR in the order of 11 W kg^{-1}. This is well illustrated by the map in Figure 2c, which represents the spatial distribution of the temperature at thermal equilibrium, calculated over a cross section of the rat (Figure 1a), for an AC magnetic field with $\hat{H}_a$ = 30 kA m^{-1} and f = 150 kHz. The temperature increments are mainly localized in proximity of the back and the abdomen, whereas the temperature within the target region is less affected by EM field exposure. As a reference, the corresponding map of the temperature due to the only metabolic heat is reported in Figure S2 in the Supporting Information.

2.2. Evaluation of Magnetic Nanoparticle Heating Effects

In the following, we investigate the combined effects of the heating due to the EM field exposure (associated with eddy current generation) and to the activation of the MNPs, assumed to be uniformly distributed within the target region Σ. The consequent temperature increase is analyzed versus the AC magnetic field parameters $\hat{H}_a$ and f, and the MNP dose, expressed as a function of the iron concentration [Fe] in Σ. This is varied in the range 0.1–5 mg cm^{-3} for all the considered types of MNPs, apart from the SPIO@dextran ones for which, due to their lower heating performance, [Fe] is varied from a minimum of 0.25 mg cm^{-3} to a maximum of 20 mg cm^{-3}, considering that larger concentrations (up to 40 mg cm^{-3}) have been already employed in in vivo tests of SPIO NPs.[44]

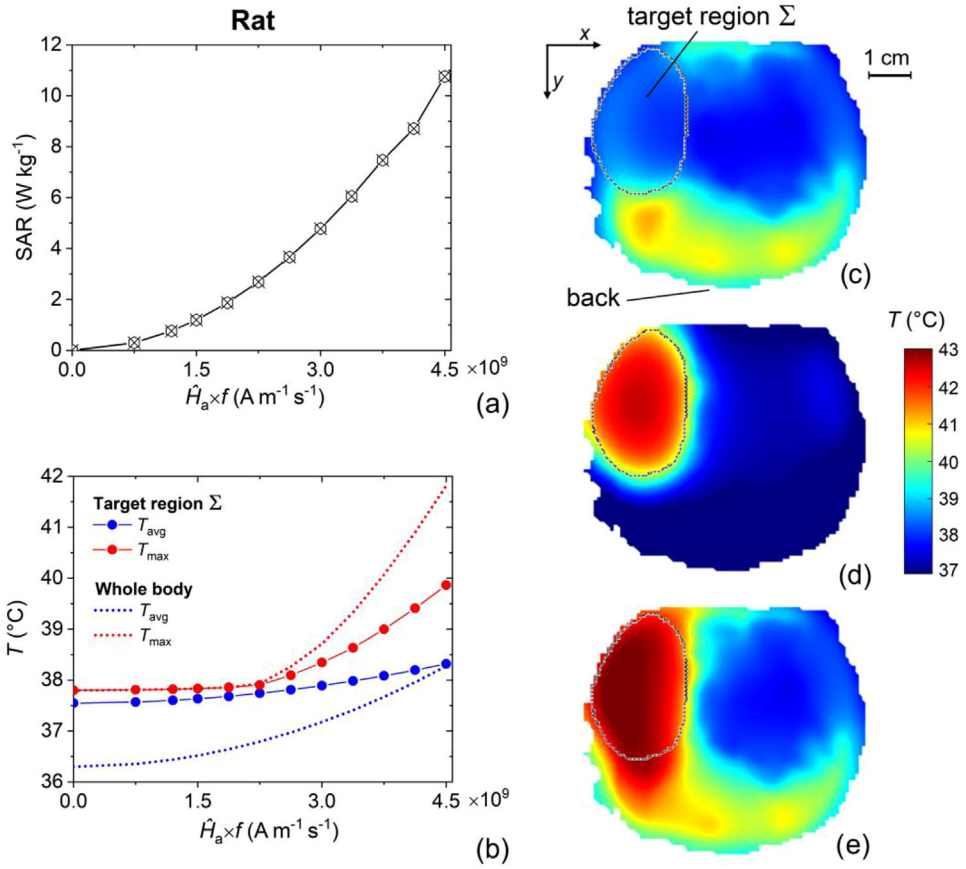

Figure 2. a) Whole-body average SAR and b) maximum and average temperatures, in the body and in the target region, estimated for the rat, versus the product of the AC magnetic field frequency and peak amplitude. The field is uniformly applied along the body's longitudinal axis. Comparison between temperature maps calculated at thermal equilibrium over the rat transversal section, depicted in blue in the schematic of Figure 1a, considering: c) the heating contribution of the only magnetic field (peak amplitude of 30 kA m^{-1} and frequency of 150 kHz), d) the heating contribution of SPIO@dextran NPs (iron concentration equal to 5 mg cm^{-3}), and e) both heating contributions. The 2D section crosses the barycenter of the tumor, whose contour is indicated by the dotted gray line.

To estimate the MNP heating efficiency in terms of thermal response, we evaluate the maximum temperature T_{max} and the average temperature T_{avg} within Σ at thermal equilibrium, and we provide a measure of the temperature uniformity through the heterogeneity coefficient HC, defined by Equation (4). The thermal equilibrium during MNP activation is reached in about 20 min, in keeping with the typical duration of mild hyperthermia treatments.[45] A time interval of 20 min is needed to re-establish the initial temperature, once the field is switched off. As an example, Figure S3 in the Supporting Information displays the heating–cooling transient when treating the mouse with SPIO@dextran NPs, fixing [Fe] to 5 mg cm^{-3}, and considering $\hat{H}_a$ = 30 kA m^{-1} and f = 150 kHz.

The four types of MNPs are compared in **Figures 3** and **4**, which show the thermal response (T_{max}, T_{avg}, and HC within Σ) calculated in the mouse and in the rat, respectively, when f is fixed to 150 kHz and $\hat{H}_a$ is varied between 8 kA m^{-1} and 30 kA m^{-1}. To simulate a real therapeutic treatment, the heating effects due to the EM field exposure are also taken into account. In the diagrams, the dashed black curves define the therapeutic temperature range of interest, i.e., 40–45 °C, for T_{avg}, whereas the dotted gray curves define the same range for T_{max}. The area of T_{max} diagram delimited by the 40 °C dashed black line and the 45 °C dotted gray line corresponds to the ideal conditions for hyperthermia treatments, where both T_{avg} and T_{max} are within the therapeutic range. We report only the results obtained with magnetic field peak amplitudes and iron concentrations leading to values of T_{avg} lower than 60 °C, in order to explore possible overheating effects for conditions slightly above mild hyperthermia, but below thermal ablation.

For each MNP type, T_{avg}, T_{max}, and HC show a similar behavior as a function of $\hat{H}_a$ and [Fe], with temperature increments that are lower in the mouse for the same magnetic field peak amplitude and iron concentration. A good level of temperature uniformity is generally found; the largest values of HC (in correspondence of T_{avg} = 60 °C) do not exceed 0.17 for the mouse and 0.14 for the rat. Within the therapeutic range, HC falls between 0.04 and 0.08 for all the MNPs, when treating the mouse, while lower values are obtained for the rat, with HC between 0.02 and 0.06.

For an easier comparison of the MNP thermal efficiency, the most significant results illustrated in Figures 3 and 4 are summarized in Figure S4 in the Supporting Information, which

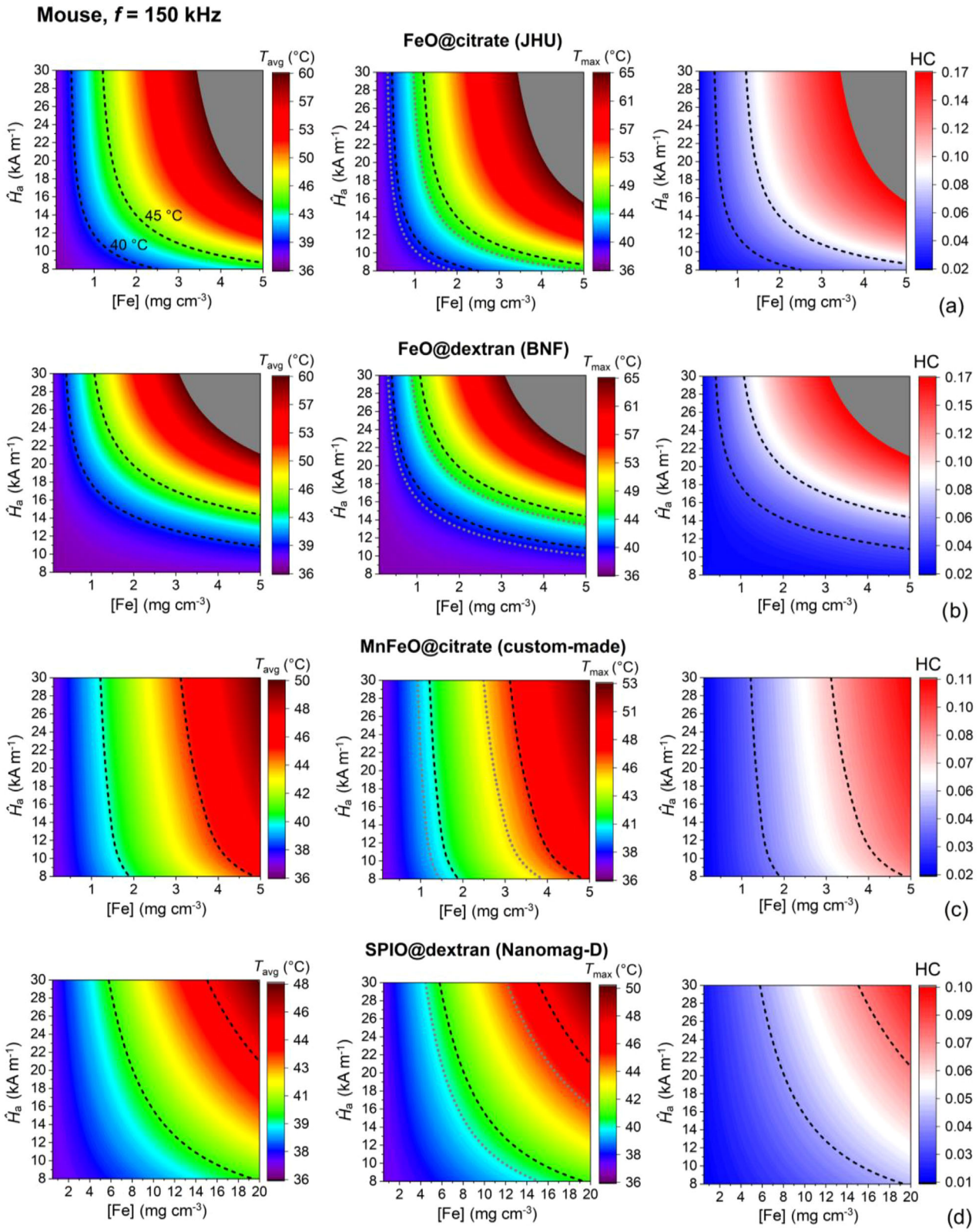

Figure 3. Diagrams of the average temperature T_{avg} (left), maximum temperature T_{max} (center), and heterogeneity coefficient HC (right) within the mouse target region, versus iron concentration [Fe] and AC magnetic field peak amplitude $\hat{H}_a$. The simulations are performed at 150 kHz, considering both EM field exposure and MNP heating contributions. The diagrams refer to a) FeO@citrate NPs, b) FeO@dextran NPs, c) MnFeO@citrate NPs, and d) SPIO@dextran NPs. The black dashed curves and the gray dotted curves delimit the temperature range of 40–45 °C for T_{avg} and T_{max}, respectively.

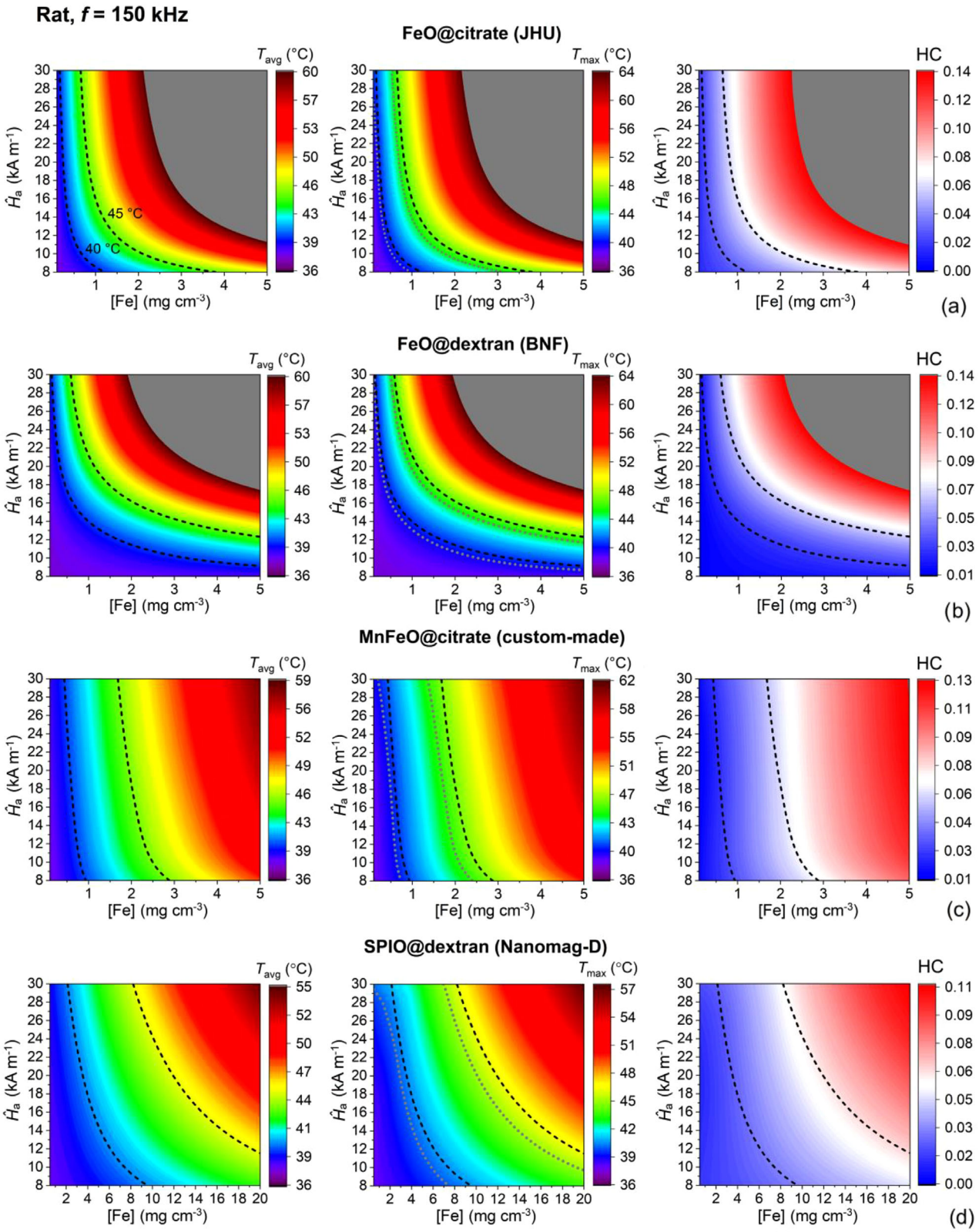

Figure 4. Diagrams of the average temperature T_{avg} (left), maximum temperature T_{max} (center), and heterogeneity coefficient HC (right) within the rat target region, versus iron concentration [Fe] and AC magnetic field peak amplitude $\hat{H}_a$. The simulations are performed at 150 kHz, considering both EM field exposure and MNP heating contributions. The diagrams refer to: a) FeO@citrate NPs, b) FeO@dextran NPs, c) MnFeO@citrate NPs, and d) SPIO@dextran NPs. The black dashed curves and the gray dotted curves delimit the temperature range of 40–45 °C for T_{avg} and T_{max}, respectively.

outlines the conditions (in terms of [Fe] and $\hat{H}_a$) for which T_{avg} = 40 °C, T_{avg} = 43 °C, and T_{max} = 45 °C in both murine models when f = 150 kHz. FeO@citrate and FeO@dextran NPs permit reaching average temperatures above 40 °C with the lowest value of [Fe], thus limiting possible toxicity effects caused by large concentration of MNPs. Specifically, this condition can be obtained in the mouse for [Fe] in the order of 0.5 mg cm^{-3} and $\hat{H}_a > 22$ kA m^{-1}, and in the rat for [Fe] in the order of 0.2 mg cm^{-3} and $\hat{H}_a > 22$ kA m^{-1} (see the graphs on the left in Figure S4, Supporting Information). With the FeO@citrate NPs the therapeutic temperature range can also be reached with much lower values of $\hat{H}_a$, at the cost of a small increase in [Fe], e.g., for $\hat{H}_a$ = 10 kA m^{-1}, it is sufficient to use an MNP dose with [Fe] around 1.3 mg cm^{-3} in the mouse and 0.6 mg cm^{-3} in the rat. On the contrary, with the FeO@dextran NPs, when $\hat{H}_a$ = 10 kA m^{-1} [Fe] should be about 3 mg cm^{-3} for the rat and higher than 5 mg cm^{-3} for the mouse. This is a consequence of the more rapid decay of the SLP of FeO@dextran NPs at 150 kHz, observed when decreasing $\hat{H}_a$ (Figure 1c).

In the large field range, MnFeO NPs are little less thermally efficient than FeO@citrate and FeO@dextran ones, while for very low fields (around 8 kA m^{-1}), they result to be the most performant ones, with an SLP higher than 100 W $g_{[Fe]}^{-1}$. With SPIO@dextran NPs, having a very small SLP (lower than 40 W $g_{[Fe]}^{-1}$), the condition of T_{avg} = 40 °C is achieved only for large values of [Fe], namely 5.8 < [Fe] < 14.4 mg cm^{-3} for the mouse and 2.1 < [Fe] < 9.5 mg cm^{-3} for the rat, when $\hat{H}_a$ is reduced from 30 kA m^{-1} down to 8 kA m^{-1}.

As shown in the central graphs of Figure S4 in the Supporting Information, a similar trend is found for T_{avg} = 43 °C, i.e., a target condition that guarantees that in all the tumor region the temperature belongs to the therapeutic range, with the minimum temperature higher than 40 °C. Overall, for the same ranges of variation of $\hat{H}_a$, when treating the mouse, the MNP dose should be practically doubled with respect to the corresponding cases for the target condition T_{avg} = 40 °C. When considering the rat, the MNP dose should be increased 2.8 times.

Attention has also to be paid in the selection of the treatment parameters, to not exceed 45 °C as a maximum temperature (see the graphs on the right in Figure S4, Supporting Information) and thus limit the appearance of side effects connected to overheating. As an example, when considering FeO@citrate NPs and [Fe] = 2 mg cm^{-3}, $\hat{H}_a$ should be lower than 12 and 9 kA m^{-1} for the mouse and rat, respectively. In general, for the same ranges of variation of $\hat{H}_a$, the critical condition of T_{max} = 45 °C can be reached by increasing 2.1 and 3.2 times the MNP dose with respect to the corresponding cases for the target condition T_{avg} = 40 °C.

As a comparison, the related diagrams of T_{avg}, T_{max}, and HC obtained with the only MNP contribution are reported in Figure S5 in the Supporting Information, for the mouse, and in Figure S6 in the Supporting Information, for the rat. It is worth noting that the thermal effects estimated in the mouse are very similar to the ones displayed in Figure 3, since the eddy current contribution due to EM field exposure is negligible in the whole body, even for the largest values of $\hat{H}_a$. On the other hand, in the rat, the eddy current contribution becomes significant also in the target region as $\hat{H}_a$ increases, and the influence is well discernible when decreasing [Fe], especially for the MNPs characterized by the lowest values of SLP at high fields, like the SPIO@dextran and MnFeO@citrate ones.

The comparison of Figure 2c–e well depicts how the heating contributions due to the MNP activation and EM field exposure affect in a different manner the spatial distribution of the temperature within the rat body. As shown in Figure 2d, the temperature increase produced by the only MNPs (SPIO@dextran NPs distributed in the target Σ region with [Fe] = 5 mg cm^{-3} for the reported case) is limited within Σ with a peak in the central area, whereas the EM field alone (Figure 2c) is responsible for a temperature increase more focused toward the back of the animal, in the fat tissue close to Σ. This contributes to a quite large extension of temperature levels above 40 °C to the healthy tissues that surround the target region, as clearly depicted by Figure 2e, where the two heating contributions are considered together. Also the temperature in Σ results to be strongly affected by the EM field exposure, with a maximum temperature increment of about 5.8 °C, against an increment of 2.9 °C due to the only MNP heating.

The SLP of the four types of MNPs greatly varies when doubling the frequency of the magnetic field. This impacts on the thermal response in the target region, as illustrated in **Figures 5** and **6**, which show the diagrams of T_{max}, T_{avg}, and HC within Σ, calculated in the mouse and in the rat, respectively, when f is fixed to 300 kHz and $\hat{H}_a$ is varied between 5 and 15 kA m^{-1}. The results in Figures 5 and 6 are summarized in Figure S7 in the Supporting Information, for the target conditions of T_{avg} = 40 °C, T_{avg} = 43 °C, and T_{max} = 45 °C. As observed for f = 150 kHz, the temperature increments are lower in the mouse than in the rat, for the same magnetic field peak amplitude and iron concentration. A good level of uniformity is obtained within the therapeutic range, which is generally achieved with smaller amounts of MNPs in comparison to the cases with f = 150 kHz, due to the increase in SLP with frequency. As an example, if we aim at reaching the condition T_{avg} = 43 °C by treating the mouse with FeO@citrate NPs excited by a magnetic field with $\hat{H}_a$ = 10 kA m^{-1}, we can advantageously reduce the iron concentration to 1.2 mg cm^{-3}, with respect to the 2.7 mg cm^{-3} value required when f = 150 kHz. When considering the rat, an iron concentration around 0.7 mg cm^{-3} can be sufficient, against a value in the order of 1.5 mg cm^{-3}.

Overall, for f = 300 kHz the most efficient MNPs result to be the FeO@citrate and MnFeO@citrate ones, with the latter that enable us to reach the therapeutic range with iron concentrations lower than 2 mg cm^{-3} for the entire interval of magnetic field peak amplitude. The FeO@dextran NPs have a stronger decay of their heating performance with the magnetic field decrease, e.g., when $\hat{H}_a$ is below 10 kA m^{-1}, [Fe] should be higher than 1.8 and 3.8 mg cm^{-3}, to guarantee the reaching of T_{avg} = 40 °C in the rat and mouse, respectively. The SPIO@dextran NPs allow to obtain an important heating contribution at significantly lower doses than for f = 150 kHz, becoming preferable to FeO@dextran NPs under specific operative conditions. Even if the Hergt-Dutz limit is again fulfilled, at the largest magnetic field amplitude, the heating effects due to the EM field exposure are no more negligible, as can be deduced by comparing Figures 5 and 6 with the corresponding diagrams depicting the heat contribution of the only MNPs, reported in Figures S8 and S9 in the Supporting Information.

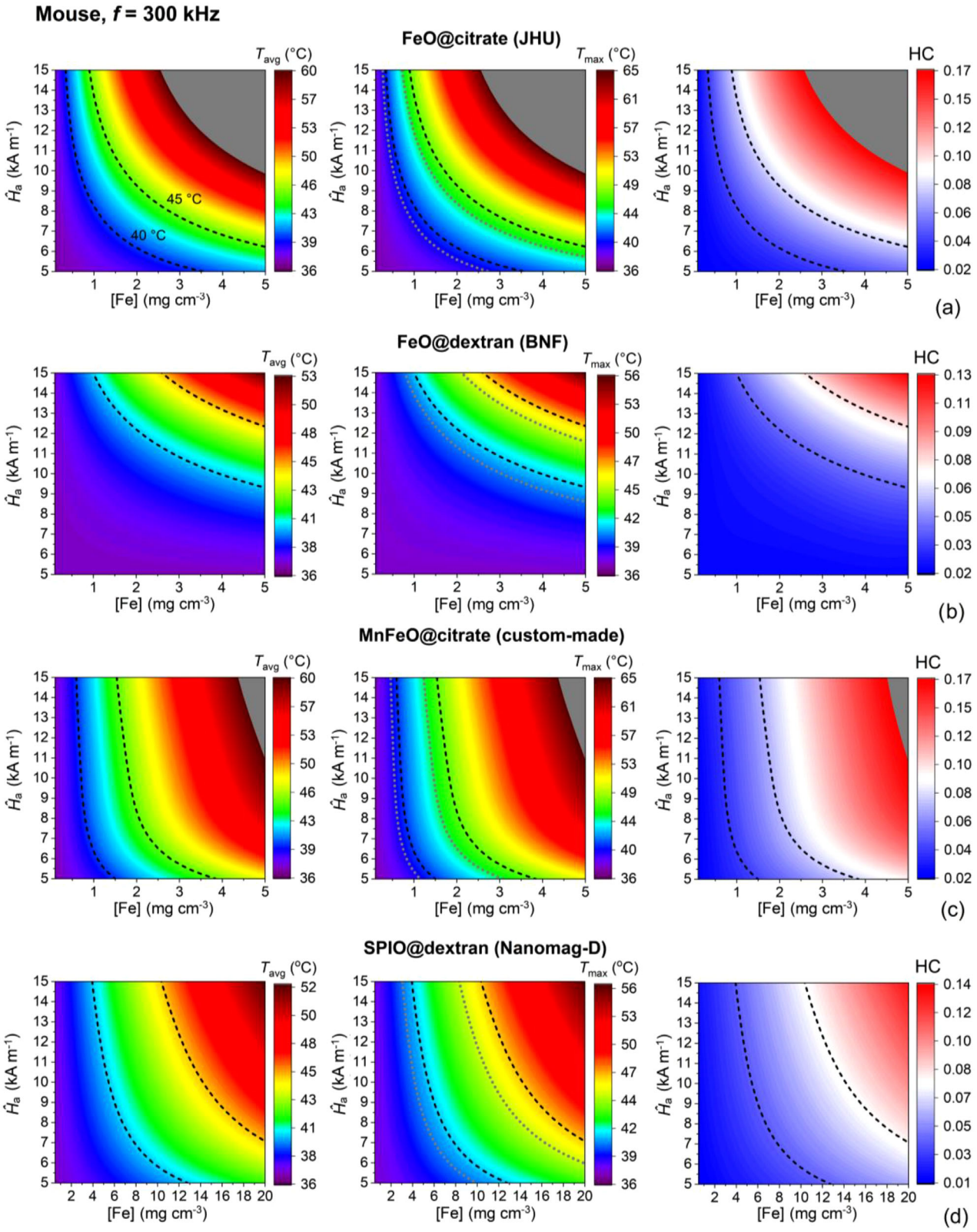

Figure 5. Diagrams of the average temperature T_{avg} (left), maximum temperature T_{max} (center), and heterogeneity coefficient HC (right) within the mouse target region, versus iron concentration [Fe] and AC magnetic field peak amplitude $\hat{H}_a$. The simulations are performed at 300 kHz, considering both EM field exposure and MNP heating contributions. The diagrams refer to: a) FeO@citrate NPs, b) FeO@dextran NPs, c) MnFeO@citrate NPs, and d) SPIO@dextran NPs. The black dashed curves and the gray dotted curves delimit the temperature range of 40–45 °C for T_{avg} and T_{max}, respectively.

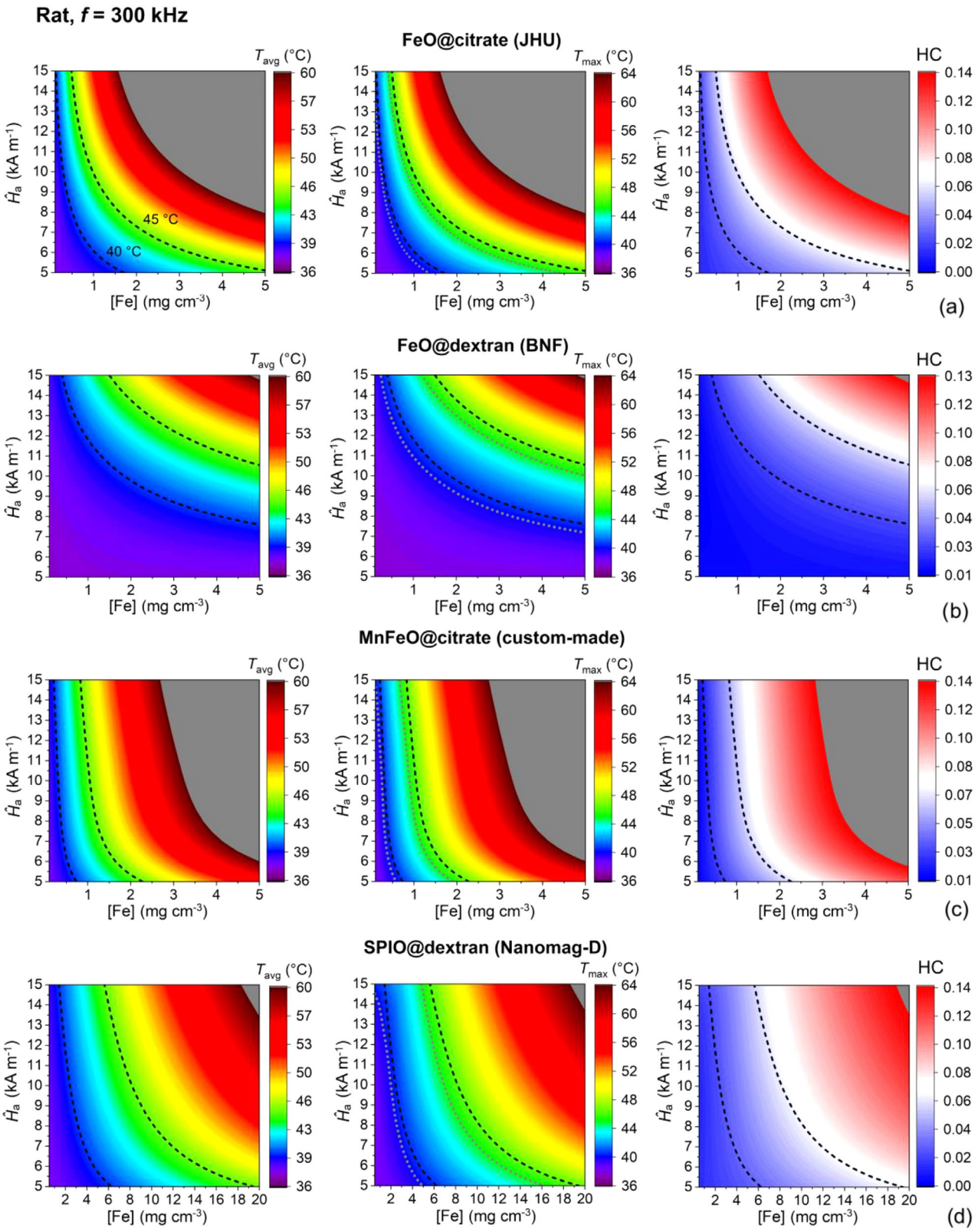

Figure 6. Diagrams of the average temperature T_{avg} (left), maximum temperature T_{max} (center), and heterogeneity coefficient HC (right) within the rat target region, versus iron concentration [Fe] and AC magnetic field peak amplitude $\hat{H}_a$. The simulations are performed at 300 kHz, considering both EM field exposure and MNP heating contributions. The diagrams refer to: a) FeO@citrate NPs, b) FeO@dextran NPs, c) MnFeO@citrate NPs, and d) SPIO@dextran NPs. The black dashed curves and the gray dotted curves delimit the temperature range of 40–45 °C for T_{avg} and T_{max}, respectively.

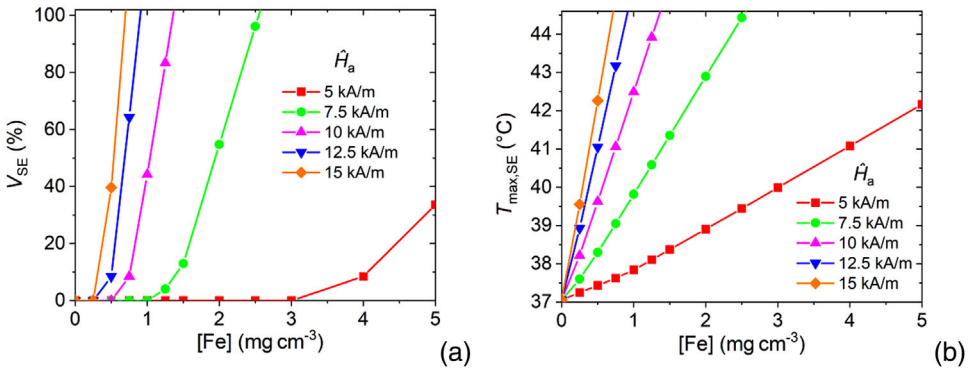

Figure 7. a) Volume fraction V_{SE} (expressed as a percentage of Σ) of the regions surrounding Σ where the temperature of 40 °C is exceeded and b) maximum temperature $T_{max,SE}$ reached there, as a function of iron concentration [Fe] and magnetic field peak amplitude $\hat{H}_a$. The simulations are performed by treating the mouse at 300 kHz with FeO@citrate NPs.

Finally, to evaluate possible side effects in the healthy tissues caused by the EM field, we determine the volume fraction V_{SE} (expressed as a percentage of Σ) of the regions surrounding Σ where the temperature of 40 °C is exceeded as well as the maximum temperature $T_{max,SE}$ reached there. For a fixed value of $\hat{H}_a$, $T_{max,SE}$ varies linearly with the iron concentration, whereas V_{SE} has an exponential-like behavior, with a zero starting plateau where the threshold of 40 °C is not overcome, and whose extension increases with the reduction in $\hat{H}_a$. This is illustrated in **Figure 7** for the FeO@citrate NPs, when used to treat the mouse at a frequency of 300 kHz; the results are reported up to the conditions that lead to $T_{max} = 45$ °C, which defines the superior limit for the ideal therapeutic range. These correspond to a maximum of 102% for V_{SE} and of 44.6 °C for $T_{max,SE}$. To reduce side effects as much as possible, very low MNP doses and small field amplitudes are required, otherwise $T_{max,SE}$ results to be in the order of the temperatures reached within the tumor, with an extension comparable with that of the target region. As an example, when $\hat{H}_a = 10$ kA m^{-1} and [Fe] = 1.25 mg cm^{-3}, in the tumor we reach $T_{avg} = 42.8$ °C and $T_{max} = 44.3$ °C, but in the surrounding tissue a temperature of 43.9 °C is found with V_{SE} around 83%, making practically unavoidable the cancellation of side effects.

In summary, the best thermal efficiency and safest treatment conditions, namely the possibility of achieving the therapeutic temperature range with the lowest MNP doses and magnetic fields, can be obtained with the FeO@citrate and MnFeO@citrate NPs, for both considered animals and treatment frequencies. In these cases, also the occurrence of side effects due to the EM field exposure is strongly limited. For a selected field peak amplitude, the MnFeO@citrate and SPIO@dextran NPs allow more flexibility in the choice of the MNP dose leading to the therapeutic temperature range, but the SPIO@dextran NPs require large amount of MNPs to reach such condition, at the cost of a possible increase in toxicity.

3. Conclusions

In this study, we have simulated in vivo experiments of magnetic hyperthermia on murine models (mice and rats) to analyze the thermal response of tumor tissues under different scenarios, depending on AC magnetic field parameters (frequency and peak amplitude), MNP heating properties and dose of MNPs administered to the tumor. In silico modeling has proven to be essential for investigating the eddy current effects due to the EM field exposure, especially for distinguishing the heating contribution of the MNPs from that of the field alone. In particular, we have demonstrated that for 30 g mice eddy current effects do not cause a noticeable temperature increase within the animal body, whereas these become important for bigger animals, like 500 g rats, also when fulfilling the Hergt-Dutz limit. In this case, to have an average temperature increment within the whole body lower than 1 °C, the product $\hat{H}_a \times f$ should not exceed the value of 3×10^9 A m^{-1} s^{-1}.

As an outcome of the simulation analysis in the presence of MNPs, we have found that for specific types of MNPs an iron concentration of 2 mg cm^{-3} within the target region can be sufficient to guarantee the reaching of the therapeutic temperature range between 40 and 45 °C in both mice and rats, with a good level of temperature uniformity. This goal can be achieved with both the JHU (FeO@citrate) and custom-made manganese ferrite (MnFeO@citrate) NPs, apart when applying very low magnetic fields corresponding to SLP values below 100 W $g_{[Fe]}^{-1}$. With BNF (FeO@dextran) NPs it is also possible to use small amount of MNPs, but more caution is needed in the selection of the magnetic field amplitude, which should be sufficiently greater (e.g., higher than 15 kA m^{-1} when treating mice) to guarantee the required temperature increase, whereas the use of Nanomag-D (SPIO@dextran) NPs demand much larger doses, apart from very restrictive heating conditions needing magnetic fields in the order of 30 kA m^{-1}.

As shown in our study, the monitoring of the temperature outside the diseased area is also important to avoid as much as possible side effects in healthy tissues surrounding the treated region. During the application of magnetic hyperthermia on mice, we have observed that when the maximum temperature inside the tumor is close to 45 °C, the nearest tissues that reach a temperature above 40 °C can occupy a volume comparable to that of the tumor itself. A much greater attention has to be paid when treating bigger animals, like rats, where higher temperatures can be reached even with smaller magnetic field amplitudes and frequencies, and lower MNP doses.

In conclusion, the obtained results have highlighted the reliability of in silico modeling in assisting in vivo experiments of magnetic hyperthermia, enabling the assessment, depending

on MNP heating properties, of the most suitable MNP dose and magnetic field parameters that can lead to temperatures in diseased tissues within the therapeutic range, avoiding the appearance of hotspots in healthy tissues at the same time.

4. Experimental Section

In the following, the numerical modeling approach that enables to evaluate the spatial-temporal distribution of the temperature within a living body, including the effects of two external heating sources, i.e., the MNPs and the AC magnetic field was described. The region occupied by the body represents the 3D domain under analysis Ω_b, where the low-frequency EM field problem and the bioheat transfer problem were solved.

Simulation of Thermal Effects: To determine the thermal effects induced in a body Ω_b, as a result of MNP excitation under an AC magnetic field, a numerical code was developed,[32] which solved the Pennes' bioheat transfer equation:

$$\rho C_p \frac{\partial T}{\partial t} = \nabla \cdot k\nabla T - WC_{blood}\,(T - T_{blood}) + Q_m + \Gamma Q_{MNPs} + Q_{EM} \quad (2)$$

where T is the local temperature, C_p is the tissue heat capacity, k is the tissue thermal conductivity, W is the tissue-blood perfusion rate, C_{blood} is the blood heat capacity, T_{blood} is the arterial temperature, Q_m is the specific metabolic heat generation rate, Q_{MNPs} is the specific heating power released by MNPs, Γ is a piecewise function equal to 1 in the tissue regions where MNPs are distributed and zero elsewhere, and Q_{EM} is the specific heating power produced by the AC magnetic field. C_{blood} and T_{blood} are fixed to 3617 J K^{-1} kg^{-1} and 37 °C, respectively. Q_{MNPs} is expressed as the product of the SLP and dose of the administered MNPs (quantified as the mass concentration of iron), whereas Q_{EM} is numerically evaluated by solving a low-frequency EM field problem with an in-house 3D FEM code.[35]

To describe the heat exchange between the skin and the surrounding environment, the following boundary condition was imposed on $\partial\Omega_b$

$$q = -k\frac{\partial T}{\partial n} = -h\,(T_{ext} - T_{skin}) \quad (3)$$

where q is the outward heat flux, T_{ext} is the external temperature (fixed to 25 °C), T_{skin} is the skin temperature, and h is the heat transfer coefficient. The initial condition (at time instant $t = 0$) corresponds to the steady-state distribution of the temperature before magnetic field application, which is governed by the metabolic heat.

After discretizing Ω_b with tetrahedral elements, Equation (2) was solved with FEM using linear shape functions and adopting the Crank-Nicholson's method for time-integration.

Application of Regression Models: The thermal effects due to MNP excitation and EM field exposure were investigated by evaluating the maximum temperature T_{max} and the average temperature T_{avg} within the treated tumor or target region, defined as Σ. To provide a measure of the temperature distribution within Σ, the following heterogeneity coefficient was also calculated

$$HC = \frac{T_5 - T_{95}}{T_{95}} \quad (4)$$

where T_5 and T_{95} are the temperatures reached within at least 5% and 95% of tumor volume, respectively. Since for each experimental condition (AC magnetic field peak amplitude and frequency, MNP type and dose), the temperature within the whole target region Σ for the evaluation of T_{max}, T_{avg}, and HC was needed to know, after the collection of a sufficient number of data, regression models were employed to complement the simulation results. The considered models were multiple linear regression (MLR) and Gaussian process regression (GPR). For the MLR, the relationship between the dependent variable and the independent ones was linear and the general equation was written as

$$y = a + \sum_{i=1}^{N} b_i \cdot x_i + \varepsilon \quad (5)$$

where y is the dependent variable to be predicted (T_{max}, T_{avg}, or HC), x_i is the ith independent variable (SLP or dose of MNPs), a is the intercept, b_i is the ith regression coefficient to be estimated, and ε is the model's error term. GPR was a nonparametric and kernel-based Bayesian model used for nonlinear regression, where the prediction was probabilistic and was formulated by means of Gaussian processes.[46] Here, the calculation was performed with the MATLAB functions *fitlm* for the MLR and *fitrgp* for the GPR, available in the Statistics and Machine Learning Toolbox.

Supporting Information

Supporting Information is available from the Wiley Online Library or from the author.

Acknowledgements

This work was supported by Project 18HLT06 RaCHy, which received funding from the European Metrology Programme for Innovation and Research (EMPIR), cofinanced by the participating states, and from the European Union's Horizon 2020 Programme. The Supporting Information was updated on July 13, 2023.

Conflict of Interest

The authors declare no conflict of interest.

Data Availability Statement

The data that support the findings of this study are available on request from the corresponding author.

Keywords

bioheat transfer model, in silico experiments, magnetic hyperthermia, magnetic nanoparticles, thermal therapies

Received: April 3, 2023
Published online: June 11, 2023

[1] H. P. Kok, E. N. K. Cressman, W. Ceelen, C. L. Brace, R. Ivkov, H. Grüll, G. Ter Haar, P. Wust, J. Crezee, *Int. J. Hyperthermia* **2020**, *37*, 711.
[2] N. R. Datta, S. G. Ordóñez, U. S. Gaipl, M. M. Paulides, H. Crezee, J. Gellermann, D. Marder, E. Puric, S. Bodis, *Cancer Treat. Rev.* **2015**, *41*, 742.
[3] J. van der Zee, Z. Vujaskovic, M. Kondo, T. Sugahara, *Int. J. Hyperthermia* **2008**, *24*, 111.
[4] S. Jha, P. K. Sharma, R. Malviya, *Life Sci.* **2016**, *10*, 161.
[5] B. Kozissnik, A. C. Bohorquez, J. Dobson, C. Rinaldi, *Int. J. Hyperthermia* **2013**, *29*, 706.
[6] M. Bañobre-López, A. Teijeiro, J. Rivas, *Rep. Pract. Oncol. Radiother.* **2013**, *18*, 397.
[7] E. A. Périgo, G. Hemery, O. Sandre, D. Ortega, E. Garaio, F. Plazaola, F. J. Teran, *Appl. Phys. Rev.* **2015**, *2*, 041302.

[8] X. Liu, Y. Zhang, Y. Wang, W. Zhu, G. Li, X. Ma, Y. Zhang, S. Chen, S. Tiwari, K. Shi, S. Zhang, H. M. Fan, Y. X. Zhao, X.-J. Liang, *Theranostics* **2020**, *10*, 3793.
[9] R. R. Wildeboer, P. Southern, Q. A. Pankhurst, *J. Phys. D: Appl. Phys.* **2014**, *47*, 495003.
[10] R. Ferrero, G. Barrera, F. Celegato, M. Vicentini, H. Sözeri, N. Yıldız, C. A. Dinçer, M. Coïsson, A. Manzin, P. Tiberto, *Nanomaterials* **2021**, *11*, 2179.
[11] H. Gavilán, K. Simeonidis, E. Myrovali, E. Mazarío, O. Chubykalo-Fesenko, R. Chantrell, L. Balcells, M. Angelakeris, M. P. Morales, D. Serantes, *Nanoscale* **2021**, *13*, 15631.
[12] R. Ferrero, A. Manzin, G. Barrera, F. Celegato, M. Coïsson, P. Tiberto, *Sci. Rep.* **2019**, *9*, 6591.
[13] H. Fatima, T. Charinpanitkul, K.-S. Kim, *Nanomaterials* **2021**, *11*, 1203.
[14] M. Vassallo, D. Martella, G. Barrera, F. Celegato, M. Coïsson, R. Ferrero, E. S. Olivetti, A. Troia, H. Sözeri, C. Parmeggiani, D. S. Wiersma, P. Tiberto, A. Manzin, *ACS Omega* **2023**, *8*, 2143.
[15] M. Cobianchi, A. Guerrini, M. Avolio, C. Innocenti, M. Corti, P. Arosio, F. Orsini, C. Sangregorio, A. Lascialfari, *J. Magn. Magn. Mater.* **2017**, *444*, 154.
[16] F. Soetaert, S. K. Kandala, A. Bakuzis, R. Ivkov, *Sci. Rep.* **2017**, *7*, 6661.
[17] W. J. Atkinson, I. A. Brezovich, D. P. Chakraborty, *IEEE Trans. Biomed. Eng.* **1984**, *31*, 70.
[18] R. Hergt, S. Dutz, *J. Magn. Magn. Mater.* **2007**, *311*, 187.
[19] H. F. Rodrigues, G. Capistrano, F. M. Mello, N. Zufelato, E. Silveira-Lacerda, A. F. Bakuzis, *Phys. Med. Biol.* **2017**, *62*, 4062.
[20] H. F. Rodrigues, F. M. Mello, L. C. Branquinho, N. Zufelato, E. P. Silveira-Lacerda, A. F. Bakuzis, *Int. J. Hyperthermia* **2013**, *29*, 752.
[21] J. Kim, S. Bae, *Sci. Rep.* **2021**, *11*, 22028.
[22] G. Capistrano, H. F. Rodrigues, N. Zufelato, C. Gonçalves, C. G. Cardoso, E. P. Silveira-Lacerda, A. F. Bakuzis, *Int. J. Hyperthermia* **2020**, *37*, 120.
[23] A. Miaskowski, M. Subramanian, *Int. J. Mol. Sci.* **2019**, *20*, 4644.
[24] A. Attaluri, S. K. Kandala, H. Zhou, M. Wabler, T. L. DeWeese, R. Ivkov, *Int. J. Hyperthermia* **2020**, *37*, 108.
[25] A. Attaluri, S. K. Kandala, M. Wabler, H. Zhou, C. Cornejo, M. Armour, M. Hedayati, Y. Zhang, T. L. DeWeese, C. Herman, R. Ivko, *Int. J. Hyperthermia* **2015**, *31*, 359.
[26] S. K. Kandala, E. Liapi, L. L. Whitcomb, A. Attaluri, R. Ivkov, *Int. J. Hyperthermia* **2019**, *36*, 115.
[27] Y. Tang, T. Jin, R. C. C. Flesch, Y. Gao, M. He, *J. Magn. Magn. Mater.* **2021**, *517*, 167391.
[28] N. D. Polychronopoulos, A. A. Gkountas, I. E. Sarris, L. A. Spyrou, *Appl. Sci.* **2021**, *11*, 9526.
[29] S. Nain, N. Kumar, P. K. Avti, *Therm. Sci. Eng. Prog.* **2022**, *34*, 101396.
[30] M. Suleman, S. Riaz, *J. Magn. Magn. Mater.* **2020**, *498*, 166143.
[31] R. Rahpeima, C.-A. Lin, *PLoS One* **2022**, *17*, e0274801.
[32] A. Manzin, R. Ferrero, M. Vicentini, *Adv. Theory Simul.* **2021**, *4*, 2100013.
[33] M. Suleman, S. Riaz, *J. Therm. Biol.* **2020**, *91*, 102635.
[34] A. LeBrun, N. Manuchehrabadi, A. Attaluri, F. Wang, R. Ma, L. Zhu, *Int. J. Hyperthermia* **2013**, *29*, 730.
[35] M. Vicentini, M. Vassallo, R. Ferrero, I. Androulakis, A. Manzin, *Comput. Methods Programs Biomed.* **2022**, *223*, 106975.
[36] IT'IS Foundation, Animal Models, https://itis.swiss/virtual-population/animal-models/animals/ (accessed: March 2023).
[37] IT'IS Foundation, Tissue Properties, https://itis.swiss/virtual-population/tissue-properties/overview/ (accessed: March 2023).
[38] A. Trakic, F. Liu, S. Crozier, *Phys. Med. Biol.* **2006**, *51*, 1673.
[39] S. Kodera, J. Gomez-Tames, A. Hirata, H. Masuda, T. Arima, S. Watanabe, *Int. J. Environ. Res. Public Health* **2017**, *14*, 358.
[40] M. Wabler, W. Zhu, M. Hedayati, A. Attaluri, H. Zhou, J. Mihalic, A. Geyh, T. L. DeWeese, R. Ivkov, D. Artemov, *Int. J. Hyperthermia* **2014**, *30*, 192.
[41] C. L. Dennis, K. L. Krycka, J. A. Borchers, R. D. Desautels, J. van Lierop, N. F. Huls, A. J. Jackson, C. Gruettner, R. Ivkov, *Adv. Funct. Mater.* **2015**, *25*, 4300.
[42] L. C. Branquinho, M. S. Carrião, A. S. Costa, N. Zufelato, M. H. Sousa, R. Miotto, R. Ivkov, A. F. Bakuzis, *Sci. Rep.* **2013**, *3*, 2887.
[43] J. M. Osepchuk, R. C. Petersen, *Bioelectromagnetics* **2003**, *6*, S7.
[44] T. J. Carter, G. Agliardi, F.-Y. Lin, M. Ellis, C. Jones, M. Robson, A. Richard-Londt, P. Southern, M. Lythgoe, M. Zaw Thin, V. Ryzhov, R. T. M. de Rosales, C. Gruettner, M. R. A. Abdollah, R. B. Pedley, Q. A. Pankhurst, T. L. Kalber, S. Brandner, S. Quezada, P. Mulholland, M. Shevtsov, K. Chester, *Small* **2021**, *17*, 2005241.
[45] L. Beola, L. Gutiérrez, V. Grazú, L. Asín, in *Nanomaterials for Magnetic and Optical Hyperthermia Applications*, Elsevier, Amsterdam, Netherlands **2019**, Ch. 12.
[46] C. E. Rasmussen, C. K. I. Williams, *Gaussian Processes for Machine Learning*, The MIT Press, Cambridge, MA **2006**.